Applied Surface Science 495 (2019) 143521

Contents lists available at ScienceDirect

Applied Surface Science

journal homepage: www.elsevier.com/locate/apsusc

Full length article

Fabrication of the flower-flake-like $CuBi_2O_4/Bi_2WO_6$ heterostructure as efficient visible-light driven photocatalysts: Performance, kinetics and mechanism insight

Liping Wang[a,b], Guangpeng Yang[b,c], Dong Wang[b], Changyu Lu[d,*], Weisheng Guan[a,*], Yuliang Li[a], Jing Deng[e], John Crittenden[b]

[a] Key Laboratory of Subsurface Hydrology and Ecological Effects in Arid Region, Ministry of Education, School of Environmental Science and Engineering, Chang'an University, Xi'an 710064, PR China
[b] Brook Byers Institute for Sustainable Systems and School of Civil and Environmental Engineering, Georgia Institute of Technology, Atlanta, GA 30332, United States
[c] School of Energy and Power Engineering, Chongqing University, Chongqing 400044, PR China
[d] Hebei Province Key Laboratory of Sustained Utilization & Development of Water Recourse, Department of Water Resource and Environment, Hebei Geo University, No. 136 Huai'an Road, Shijiazhuang 050031, Hebei, PR China
[e] College of Civil Engineering and Architecture, Zhejiang University of Technology, Hangzhou 310014, PR China

ARTICLE INFO

Keywords:
$CuBi_2O_4$
Bi_2WO_6
Z-scheme
Tetracycline photodegradation

ABSTRACT

Effective sunlight harvesting to realize environmental remediation remains great challenge for photocatalysis technique. Herein, the visible-light-driven $CuBi_2O_4/Bi_2WO_6$ hierarchical nanocomposites were synthesized via a facile hydrothermal method. Compared to the pristine $CuBi_2O_4$ and Bi_2WO_6, all the $CuBi_2O_4/Bi_2WO_6$ nanocomposites exhibited the superior photocatalytic activity toward tetracycline (TC) degradation under visible light irradiation ($\lambda > 420$ nm). Particularly, 60 wt% $CuBi_2O_4/Bi_2WO_6$ nanocomposite displayed the best photocatalytic activity, which can degrade 93% TC (20 mg/L) in 1 h with the rate constant of 0.0286 min^{-1}. Based on the COD removal, the apparent quantum yield was calculated to be 0.32%. The superior photocatalytic performance of the $CuBi_2O_4/Bi_2WO_6$ nanocomposite is mainly attributed to: **I**) the efficient interfacial charge separation of the Z-scheme heterojunction; **II**) the prolonged lifetime of the charge carriers; **III**) the enlarged hierarchical surface area; **IV**) the strengthened visible light absorption. The DFT calculations suggested that the photoexcited electrons were transferred from the Bi_2WO_6 conduction band consisting of W5d orbital to recombine with the holes in the $CuBi_2O_4$ valence band consisting of O2p orbital of, which greatly facilitated the charge separation in the heterostructure. This study could provide some enlightment to the heterojunction construction and visible light utilization for other catalytic system.

1. Introduction

Tetracycline (TC), as a broad-spectrum antibiotic, is extensively used to treat infections in humans, animals and aquaculture [1]. However, TC possesses high structural stability and resistance, making it quite difficult to be metabolized by human body and to be degraded in the natural environment [2,3]. The chronic accumulation of TC has posed serious threat not only to the human health but also to the ecological systems [4]. In recent years, several conventional remediation technologies have been applied to the elimination of TC from wastewater, such as adsorption [5], chem-electrolysis [6], membrane filtration [7].etc. These treatment methods are restricted to some extent due to the economic-inefficiency and operational difficulties. Semiconductor-based photolysis is considered as a promising method for TC removal in wastewater, because of its advantage of high efficiency, low secondary pollution and cost-effectiveness [8,9]. However, most conventional photocatalysts, such as the hot-star semiconductor TiO_2 (band gap 3.2 eV) [10], ZnO (3.2 eV) [11], ZnS (3.6 eV) [12].etc. can only be irradiated by UV light, which comprises < 5% of the sunlight [13]. Hence, it is imperative to explore novel visible-light-driven semiconductors with optimized band gap, which is the priority problem of photocatalysis technology.

Bismuth tungstate, as a visible-light-driven photocatalytic semiconductor, Bi_2WO_6 (BWO) has attracted a great deal of interest because it is non-toxic, efficient, and stable [14]. Its smaller band gap (~2.7 eV) enables it to absorb visible solar light. In recent years, BWO has been

* Corresponding authors.
E-mail addresses: pzpzlxl@163.com (C. Lu), guanweisheng@263.net (W. Guan).

https://doi.org/10.1016/j.apsusc.2019.07.263
Received 27 May 2019; Received in revised form 9 July 2019; Accepted 29 July 2019
Available online 30 July 2019

widely used in organic pollutants oxidization [15], hydrogen generation [16], and CO_2 reduction [17]. The superior properties of BWO can also be ascribed to its unique structure that the octahedron of ceratoid WO_6 exists in the sandwich of $(Bi_2O_2)^{2+}$, which can promote the separation of photo-generated charges [18]. However, the pristine BWO still needs further improvement on its photocatalytic performance because its band gap is still too large for sufficient visible light utilization. The bulk BWO still suffers from a high rate of electron-hole recombination, poor charge carriers transport property and relatively low quantum efficiency [19]. Coupling BWO with other semiconductors having suitable band position to construct heterojunction system can be adopted to improve its photocatalytic activity [20,21].

Nowadays, the construction of direct Z-scheme heterojunction has greatly drawn researchers' attention. The unique interface of the Z-scheme heterojunction can not only improve the separation efficiency of the photogenerated electron-hole pairs spatially, but also retain the prominent redox potential of the photocatalyst [22,23]. Typically, for Z-scheme photocatalysts, the electrons from the less negative conduction band (CB) of one semiconductor will directly recombine with holes from the less positive valence band (VB) of another semiconductor [24]. Accordingly, the electrons left in the more negative CB had stronger reduction potential, and the holes left in the more positive VB had higher oxidation potential. Thus, Z-scheme heterojunction retains stronger reduction and oxidation ability of each semiconductor [25,26]. For example, Yan et al. constructed a Z-scheme type $BiOIO_3$/g-C_3N_4 hybrids, which exhibited significantly improved photocatalytic activities toward 2,4,6-trichlorophenol oxidation and hydrogen evolution for water splitting [27]. Zhao et al. fabricated a novel Z-scheme Ag_3VO_4/$BiVO_4$ heterojunction photocatalyst for the efficient reduction of Cr^{6+} and oxidation of Bisphenol S using visible light [28]. Thus, constructing a direct Z-scheme heterojunction with BWO is a promising pathway to improve its photocatalytic performance and quantum efficiency.

By now, many semiconductors have been chosen to fabricate heterojunctions with BWO. For example, Sun et al. synthesized Bi_2WO_6/$BiPO_4$ Z-scheme photocatalysts exhibiting an enhanced dye discoloration rate, which was 1.88 times and 4.29 times higher than those of Bi_2WO_6 and $BiPO_4$ [29]. Wang et al. prepared BiOI/Bi_2WO_6 photocatalyst on activate carbon fiber and found that 20% mol BiOI/Bi_2WO_6/ACF displayed the best performance, which was 2.4 times higher than Bi_2WO_6 [30]. Few studies reported BWO cooperated with semiconductors with a narrow band gap and negative conduction band potential. Additionally, the photocatalytic activity enhancement factor of the reported composites was rarely excess 5 times higher than the bare BWO. $CuBi_2O_4$ (CBO) is an outstanding visible-light-driven photocatalyst because it has narrow band gap (1.8 eV), which contributes to its strong absorption ability in visible light region [31]. Moreover, the CB potential of CBO (–0.6 eV vs. NHE) is negative enough to drive most of the reduction reactions thermodynamically [32]. Unfortunately, single CBO exhibits poor photocatalytic performance and has a low quantum yield due to its narrow band gap. In contrast, BWO has a higher positive oxidation potential (–3.2 eV vs. NHE) for VB holes, which results to increased oxidation ability [10]. Theoretically, if CBO and BWO are combined together to form Z-scheme heterojunction on the interface, electrons will accumulate in CBO's CB, and holes will accumulate in BWO's VB. Consequently, it can make the best use of electrons' strong reduction potential and the holes' strong oxidation potential. Furthermore, the conduction potential of CBO (–0.6 eV vs. NHE) is more negative than the potential of O_2/$\cdot O_2^-$ (–0.33 eV vs. NHE), which implies that O_2 can be reduced to generate $\cdot O_2^-$. The valence potential of BWO (3.2 eV vs. NHE) is more positive than the potential of H_2O/$\cdot$OH (2.74 eV vs. NHE), and this implies that thermodynamically H_2O can be oxidized to generate $\cdot$OH. Generally, both of $\cdot O_2^-$ and $\cdot$OH radicals play critical roles in the target compound degradation and dramatically increase the pollutant' degradation rates [33–35]. Additionally, the narrow band gap of CBO makes it easier for the nanocomposites to absorb visible light. The synergistic effect between CBO and BWO should broaden the spectral response range as well as the charges separation efficiency. The efficient electron mobility of metal oxides and the complementary band edge enable an efficient electron-hole separation under Z-scheme band alignment. Benefited from the synergistic effect, the photocatalytic performance enhancement factor of the composites is expected to be greatly improved compared to the bare samples [36]. Up to now, CBO was mainly used as the photocathode material or as florescent materials. Few researches have applied CBO as co-catalyst in pollutants photocatalytic system. Therefore, we rationally synthesized a CBO/BWO nanocomposite system with Z-scheme heterojunction and we try to unveil the specific electron-hole pairs transfer route based on the electronic band structures.

In this work, a flower-flake-like CBO/BWO nanocomposites were synthesized via a facile hydrothermal method. The as-synthesized nanocomposites were systematically characterized, and their photocatalytic performance was investigated by TC degradation using visible-light irradiation ($\lambda > 420$ nm). The density of states (DOS) and electronic band structure of CBO and BWO were calculated by the plane-wave-density function theory (DFT) method. Moreover, the dominant active species were identified through the radical species trapping experiment. Based on the characterization and ESR results, two possible photocatalytic mechanisms of visible-light-driven CBO/BWO nanocomposite system were proposed and discussed in detail.

2. Experimental section

2.1. Preparation of the photocatalysts

2.1.1. Synthesis of CBO and BWO

All chemicals used in the present work were analytical grade and were used without any further modification. The CBO powder was prepared according to the previously reported hydrothermal method [37]. Sodium tungstate dehydrate ($Na_2WO_4{\cdot}2H_2O$) was used as the precursor of BWO and acetic acid was used to control its size and morphology of the BWO [38]. The specific preparation process was described in the Supplementary information.

2.1.2. Synthesis of CBO/BWO nanocomposites

In this study, the CBO/BWO nanocomposites were synthesized by a facile hydrothermal method. The basic steps were depicted in Fig. 1. The former steps were exactly the same as the synthesis process of BWO. Subsequently, after the homogeneous precursor solution of BWO was prepared, different mass of CBO (0.140 g, 0.280 g, 0.419 g, 0.558 g) were added into the above solution respectively and stirred at room temperature for 30 min. Then the obtained mixture was ultrasonically dispersed until uniformity for another 30 min. The resulted mixture was transferred into four 100 mL Teflon-lined autoclaves and heated in the oven at 180 °C for 24 h. The remaining steps were the same as above. Finally, the CBO/BWO nanocomposites were obtained, which were labeled as 20 wt% CBO/BWO, 40 wt% CBO/BWO, 60 wt% CBO/BWO and 80 wt% CBO/BWO, respectively.

2.2. Characterization

The detailed characterization was in Supplementary Information (Seeing SI 2.2).

2.3. Photocatalytic activity measurement

Briefly, 50 mg photocatalyst was suspended in a 50 mL TC aqueous solution (20 mg/L). Before irradiation, the solution was magnetically stirred for 30 min in dark to achieve adsorption-desorption equilibrium. A 300 W xenon lamp (cutting off $\lambda < 420$ nm) was employed as the visible light source. During light irradiation, 4 mL suspension was

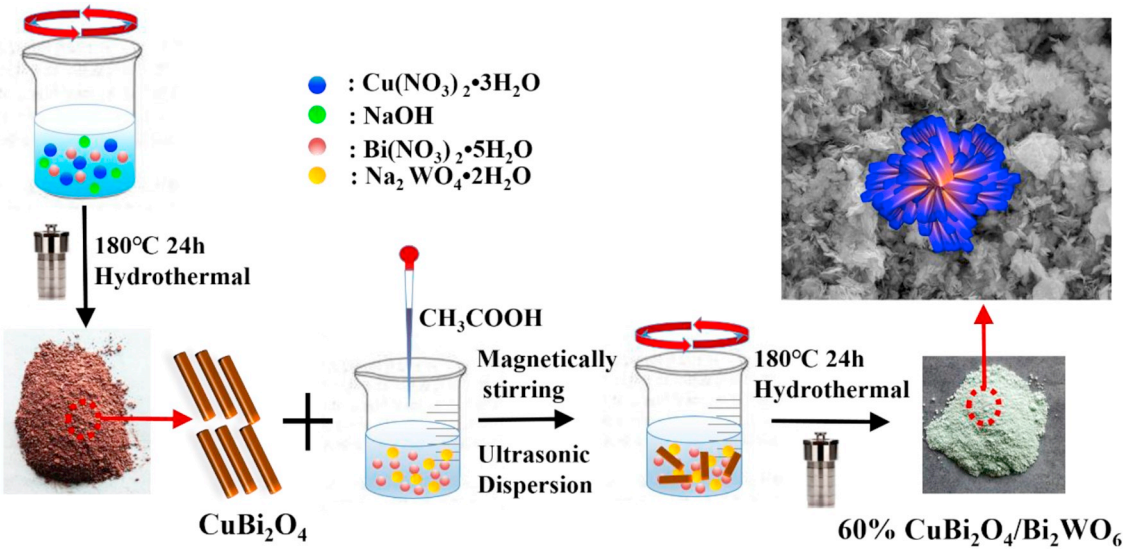

Fig. 1. Schematic of CBO/BWO nanocomposites preparation.

withdrawn at certain time intervals, and was centrifuged to separate the photocatalyst out of the solution. Then the absorbance of the solution was analyzed by UV–vis spectrophotometer at 357 nm.

2.4. Active species capturing and ESR experiments

The active species capturing experiments were performed under the same conditions. Sacrificial agents such as 2-propanol (IPA), disodium ethylene-diamine tetra acetic acid (EDTA) and 1,4-benzoquinone (BQ) were used as quencher for hydroxyl radicals (·OH), holes (h^+) and superoxide radicals ($\cdot O^{2-}$), respectively. This method was similar to the preceding photocatalytic activity test, except that 1 mM scavenger was added. In addition, the ESR technique was applied to further detect the presence of ·OH and $\cdot O^{2-}$ in the photocatalytic reaction system. The generated ·OH and $\cdot O^{2-}$ can be trapped by 5,5-Dimethyl-1-pyrroline N-oxide (DMPO) to form corresponding adducts, which can be detected using ESR spectrometer.

2.5. Computational details

The density functional theory (DFT) calculations were performed using CASTEP code in Materials Studios 8.0. Generalized gradient approximation (GGA) using Perdew-Burke-Ernzerhof (PBE) form was applied to describe the electron exchange and correlation. The cutoff was set at 600 eV for all the calculations. The ultrasoft pseudopotential was used for core and valence states. The k-points were set as 3 × 1 × 3 for the Bi_2WO_6 supercell, and 2 × 2 × 2 for the $CuBi_2O_4$ supercell. The convergence tolerance energy was converged to 10^{-6} eV/atom, the configuration was regarded as fully relaxed when the force was < 0.05 eV/Å, and the maximum displacement was 0.001 Å.

3. Results and discussions

XRD was applied to characterize the crystal structure of as-synthesized photocatalysts. The XRD patterns of the pure CBO, BWO and CBO/BWO nanocomposites are shown in Fig. 2a. All the diffraction peaks of pure CBO and BWO are in good agreement with their tetragonal phase (JCPDS No. 72-0493) and orthorhombic phase (JCPDS No. 39-0256). Additionally, the pure BWO has four obvious peaks at 28.3°, 32.8°, 47.1° and 55.8°, which can be ascribed to (131), (200), (202) and (331) diffraction planes, respectively. Furthermore, the intensity of these characteristic peaks decreased gradually with the increasing mass ratio of CBO in the nanocomposites, and finally overlapped with (211), (310), (411) and (332) diffraction planes of CBO. Particularly, for 60% nanocomposite, the peak of CBO (211) plane and BWO (131) plane overlapped. And the new peak became broader and the position slightly shifted to the right for ~0.5°, which can be explained by CBO nanorod inserted into the [WO_6] layers of precursor of BWO under high temperature and pressure. These overlapped peaks might be attributed to the formation of heterojunction between CBO and BWO. As for pure CBO, typical (211) and (411) diffraction planes located at 27.9° and 46.6° can be observed. No other impure peaks are observed in the composites, indicating that the CBO/BWO heterostructures has been successfully synthesized without any impurities.

FT-IR was used to analyze the functional groups of the as-prepared photocatalysts. In Fig. 2b, the adsorption peaks of pure BWO mainly range from 500 to 800 cm^{-1}, which can be ascribed to Bi—O stretching, W—O stretching and W—O—W bridging stretching modes [39]. With the decreasing mass ratio of CBO in CBO/BWO nanocomposites, the absorption bands at 500–800 cm^{-1} become more obvious, indicating the existence of BWO in the hybrids. The characteristic absorption peak of BWO and CBO/BWO nanocomposites at 1640 cm^{-1} and 3450 cm^{-1} in the region 3200–3600 cm^{-1} are attributed to O—H bending vibrations, which stems from the adsorbed water molecules. These peaks become stronger as BWO ratio increases. The O—H group can be scavenged by the photoinduced holes to generate the powerful hydroxyl radicals · OH, which can efficiently oxidize the organic compounds [40]. Additionally, there is a quite weak peak located at 1384 cm^{-1} due to the vibration of N—O, coming from the raw material of $Bi(NO_3)_3{\cdot}5H_2O$ [41]. An obvious absorption peak located at 1398 cm^{-1} can be observed from the spectrum of CBO, which is assigned to stretching vibration of Bi—O bonds [42]. Another peak presented at 497 cm^{-1} can be ascribed to the stretching vibration of Cu—O bonds [43]. These main absorption peaks of CBO could also be observed in all CBO/BWO nanocomposites. The FT-IR results further indicate that the function groups and structures of CBO and BWO have not changed in CBO/BWO nanocomposites.

To investigate the morphology and structure of the as-prepared samples, SEM images and EDS spectra were employed and the results were displayed in Fig. 3. Fig. 3a and b shows that pure BWO exists as an irregular pseudo-sphere-like microstructures with an average diameter of about 200 nm. BWO displays good dispersion without obvious agglomeration. The typical morphologies of CBO are displayed in Fig. 3c and d. Apparently, pure CBO has a microrod-like morphology with an average diameter of around 60 nm, and a length about 2 μm. Fig. 3e and f displays the morphology and structure of 60% CBO/BWO

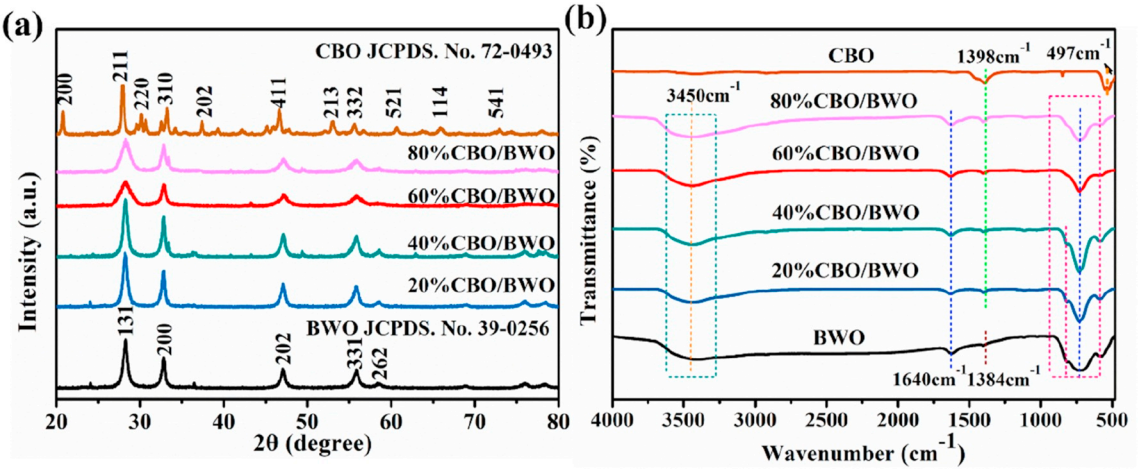

Fig. 2. (a) XRD patterns and (b) FT-IR spectra of the pure CBO, BWO and CBO/BWO nanocomposites.

nanocomposite at different magnifications. It can be clearly seen, after CBO and BWO were combined, the morphology of the nanocomposite completely changed. The morphology of 60% CBO/BWO nanocomposite didn't resemble the morphology characteristic of pure BWO or CBO. It appeared as a hierarchical flake-flower-like nanosheets and the nanosheets were assembled together. The assembled-nanosheets were uniformly dispersed. The average diameter of the nanosheets was about 200 nm. The EDS test was also performed to confirm the elemental composition of the nanocomposite. The EDS results shown in Fig. 3g reveal that 60% CBO/BWO sample contains only Bi, O, W and Cu elements. The EDS elemental mapping in Fig. 3h displayed a homogeneous distribution of Bi, W, Cu and O elements in 60% CBO/BWO nanocomposite. The EDS results demonstrate that there are no impurities (elements) in the as-prepared nanocomposites. The unique morphology and structure of CBO/BWO nanocomposite might resulted from the complex interaction of CBO and the precursor solution of BWO under high temperature and pressure in the hydrothermal synthesis process, which modified the morphology of the pristine materials.

TEM was performed to unveil the detailed particle structure and morphology of CBO/BWO nanocomposite. As shown in Fig. 4a and b, the CBO/BWO nanostructure consists of interlaced nanosheets, and agglomeration phenomenon appears in some spots. The detailed structure information of 60% CBO/BWO sample was further investigated using HR-TEM (Fig. 4c). Lattice spacing distance was calculated by the Fourier transform diffraction pattern in Fig. 4d. The calculated lattice spacing is 0.273 and 0.420 nm, which is corresponded to the (200) plane of BWO and (200) plane of CBO, respectively.

XPS spectra were conducted to reveal the surface elemental compositions and chemical states of the as-prepared samples. Fig. 5 exhibits the survey of the obtained 60% CBO/BWO nanocomposite and high-resolution XPS spectra of the Cu 2p, Bi 4f, O 1s, W 4f and C 1s. The XPS spectra reveals that the 60% CBO/BWO nanocomposite mainly contains Cu, Bi, O and W elements, which agrees well with EDS results. The observed C signal arises from carbon that is added to the sample and is used for calibration of the binding energy scale [44]. In the Cu 2p XPS spectra shown in Fig. 5b, the peaks at 933.1 and 953.2 eV are attributed to the binding energies for Cu 2p3/2 and Cu 2p1/2, respectively. The peaks at 942.5 and 962.6 eV are the satellite peaks of Cu 2p. The Cu 2p peak positions and the presence of satellite peaks confirm that the copper species exists as the featured characteristics +2 oxidation state in CBO [44]. In the high resolution spectrum of Bi 4f (Fig. 5c), the Bi 4f5/2 and Bi 4f7/2 are located in 164.2 and 158.9 eV, which are the featured characteristics of Bi^{3+} in BWO [45]. The O 1s spectrum in Fig. 5d exhibits the binding energy at 529.9 eV, which is ascribed to the crystal lattice oxygen (O^{2-}) in the CBO/BWO nanocomposite. The peaks at higher binding energies 530.9 eV could possibly be aroused by the contribution of surface defects or chemisorbed oxygen species [13,44]. In the spectrum of W 4f (Fig. 5e), two peaks at 35.1 and 37.2 eV correspond to the characteristic W 4f7/2 and W 4f5/2 peaks for BWO, respectively [46], which indicates the existence of W^{6+} in the nanocomposite. Thus, these results further confirmed the co-existence of CBO and BWO in the heterostructures.

The optical absorption properties of the as-prepared samples were obtained by the UV–vis DRS. In Fig. 6a, the absorption edge for pure CBO is extended to > 700 nm, confirming CBO is a visible-light-driven photocatalyst, which is in agreement with the previous research [37]. Compared with the pure BWO, whose absorption edge is 460 nm, 60% CBO/BWO nanocomposite exhibits a significant redshift advancement. The strong light harvesting property of CBO contributes a lot to the obvious visible light absorption enhancement of 60% CBO/BWO nanocomposite. While for other ratios of CBO/BWO nanocomposites, the absorption enhancement in the visible light region didn't manifest obviously. The band gap energy of the as-prepared samples could be calculated by the following formula:

$$\alpha h\nu = A(h\nu - E_g)^{n/2} \quad (1)$$

where α, h, ν, A, E_g and n represent the absorption coefficient, Planck constant, irradiation frequency, absorption constant, gap energy and a constant, respectively [47]. The E_g values of the as-prepared samples were determined by the plots of $(\alpha h\nu)^2$. As shown in Fig. 6b, the band gap of BWO and CBO was calculated to be 2.7 eV and 1.8 eV, which was consistent with the previous reports [48,49]. Noticeably, the band gap of 60% CBO/BWO was 2.2 eV. The composite's band gap was greatly narrowed after combined the narrow-band-gap CBO with the wide-band-gap BWO, which essentially explained the strengthened visible light absorption of 60% CBO/BWO nanocomposite. The CB and VB potentials of the two semiconductors can be predicted by the following empirical equations:

$$E_{CB} = \chi - E^e - 0.5E_g \quad (2)$$

$$E_{VB} = E_{CB} + E_g \quad (3)$$

where E_{CB} is the CB energy; χ is absolute electronegativity of CBO and BWO; E^e (4.5 eV) is the energy of free electrons with the hydrogen scale [50]. The X values for CBO and BWO are 4.75 eV and 6.39 eV, respectively [51]. The calculated CB and VB potentials of CBO and BWO are shown in Table S1, which was consistent with the theoretical value.

The photocatalytic activity of the semiconductor significantly depended on its energy level and the band gap. In our work, the electronic band structures of BWO and CBO were investigated by DFT calculations shown in Fig. 7. The occupied bands of BWO and CBO were classified into four and three bands, respectively. For BWO, from lower-energy to

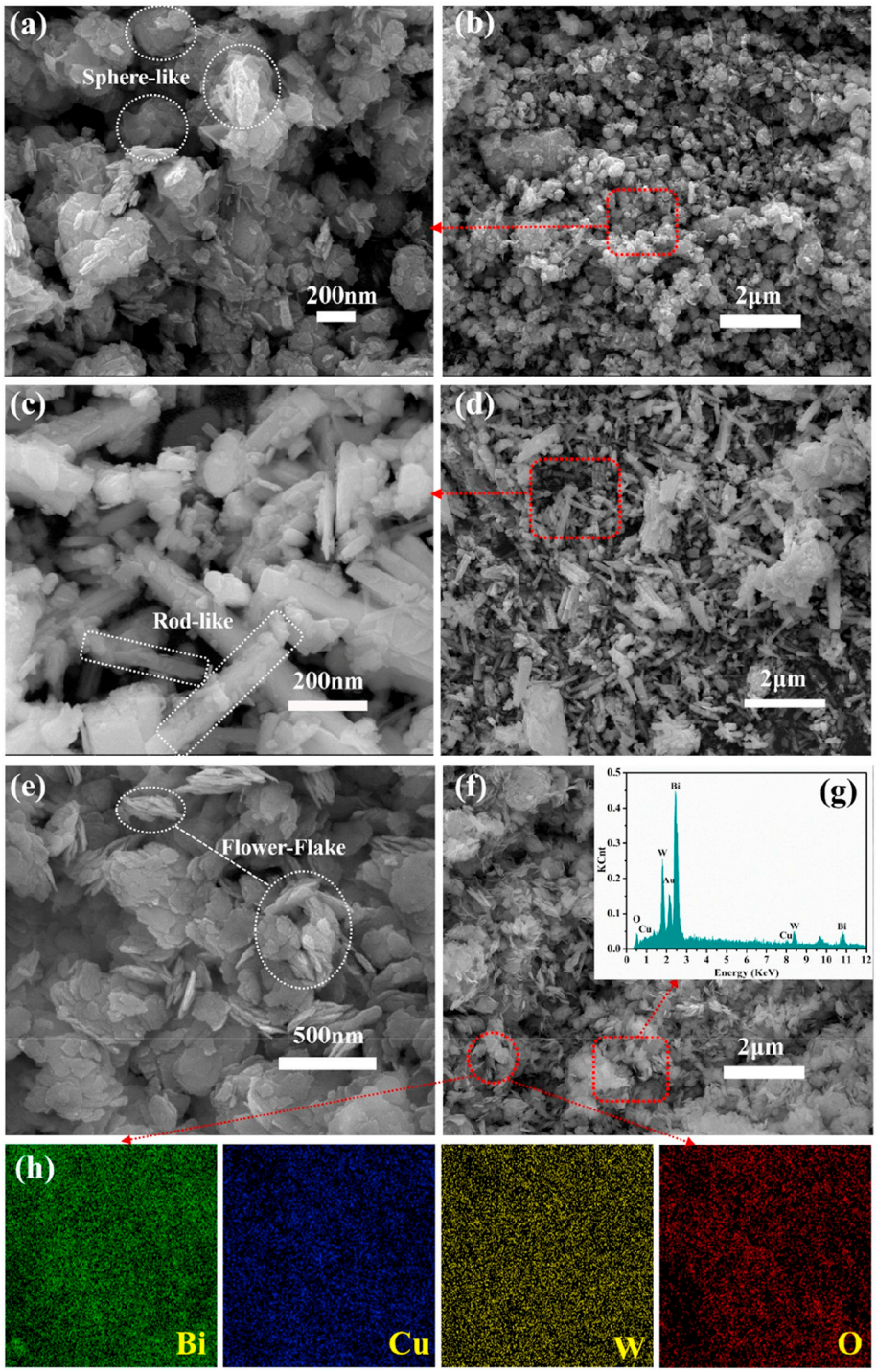

Fig. 3. SEM images of (a), (b) pure BWO; (c), (d) pure CBO; (e), (f) 60% CBO/BWO; (g) the corresponding EDS spectra of 60% CBO/BWO; (h) the EDX elemental mapping images of 60% CBO/BWO.

higher-energy side, the occupied bands consisted of solely O2s, Bi6s orbitals, O2p + Bi6p + W5d and O2p + Bi6s hybrid orbitals. The bottom of the conduction band was composed of the W5d, and a small part of O2p and Bi6p orbitals. Thus, it can be concluded that the highest occupied orbital level was formed by the hybrid orbitals of O2p and Bi6s, and lowest unoccupied molecular orbital level was the W5d orbitals. These results indicated that the photoexcitation electrons transfer from the valence band formed by O2p + Bi6s hybrid orbitals to the conduction band of W5d orbital. The band gap of BWO was calculated to be 2.15 eV. Generally, the band gap simulated by DFT method was narrower than the experimental result (2.7 eV), which may be stemmed from the well-known GCA limitation [52]. While for CBO, from lower-energy to higher-energy side, the occupied bands consisted of solely O2s, Bi6s orbitals and O2p + Cu3d + Bi6p hybrid orbitals. The valence and conduction band edges of CBO were produced by the combination of O2p and Cu3d orbitals, respectively. The energy of p-d transition from the valence band edge of O2p to the conduction band edge of Cu3d was calculated to be 1.82 eV, which agreed well with that measured by UV–vis in Fig. 6. The atom structure model of the BWO and CBO was depicted in Fig. 7c and f. In the BWO structure model, the W atom are coordinated with 6 O atoms, indicating that W exists as WO_6 octahedral layer, which is consistent with the XPS results that W

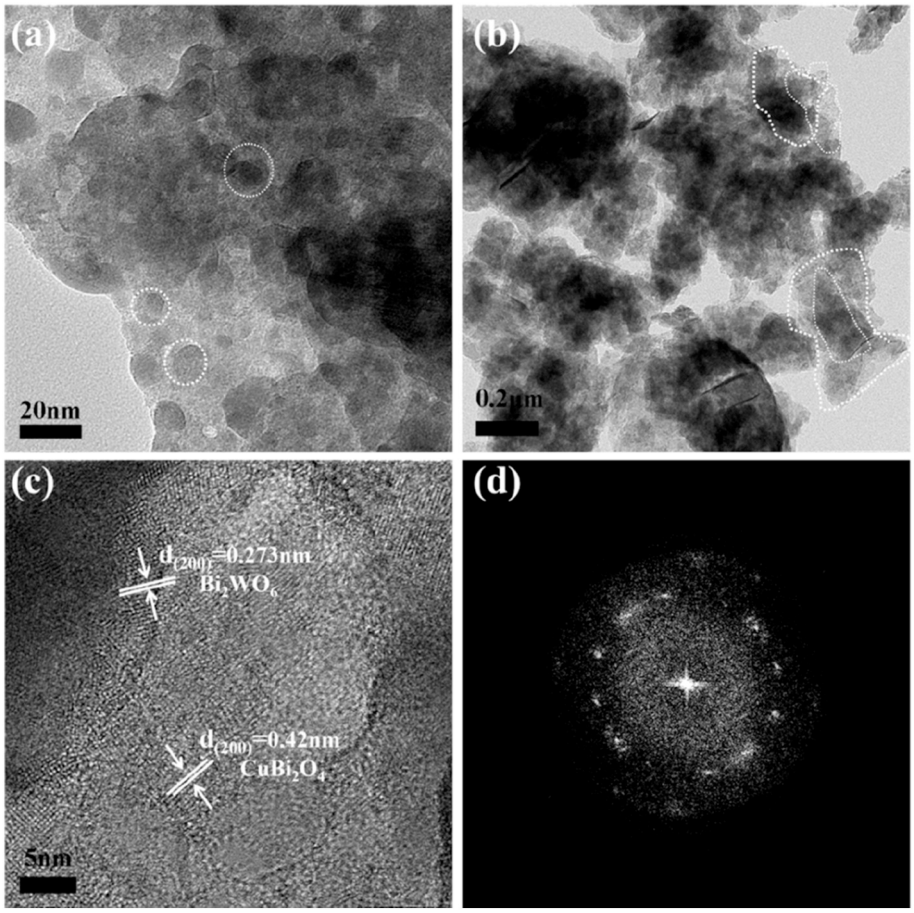

Fig. 4. (a) (b) TEM, (c) HRTEM images and (d) Fourier transform Diffraction pattern of 60% CBO/BWO nanocomposite.

exists in +6 oxidation state. The WO_6 octahedral layer connected to each other by corner-sharing O atom, and interlaced to the sandwich of $(Bi_2O_2)^{2+}$, which has been proved that this specific structure is favorable to visible-light response [53]. In the CBO structure model, the Cu and Bi atom are both coordinated with 4 O atoms, constituting the square-planar CuO_4^{6-} complexes which facilitate the charge transfer in CBO crystal structure. The DFT calculations disclose the basic electronic and band structure of CBO and BWO, which helps us further understand the charges transfer route based on the orbital level.

The specific surface area, pore volume and average pore diameter of CBO, BWO and 60% CBO/BWO are summarized in Fig. 8a. Obviously, the samples display typical type IV isotherms curves with type H3 hysteresis loop, which is consistent with the demonstration in Fig. 8b that the as prepared samples possess a mesoporous structure [54,55]. The average pore diameter of as-prepared CBO, BWO and 60% CBO/BWO samples are similar, which are 2.74 nm, 2.40 nm, 2.52 nm, respectively. Notably, 60% CBO/BWO nanocomposite exhibited much higher BET surface area (289.18 $m^2 g^{-1}$) than pristine CBO (40.56 $m^2 g^{-1}$) and BWO (63.41 $m^2 g^{-1}$), which is in great accordance with the adsorption ability of the as-prepared samples. The adsorption efficiency of as-prepared samples in dark was illustrated in the column graph inserted in Fig. 8b. It can be seen from the inserted bar graph that CBO/BWO nanocomposites possess excellent adsorption ability compared to the pristine samples. The adsorption efficiency of 60% CBO/BWO was approximately two times higher than that of bare CBO and BWO. Essentially, BET results well explained different adsorption ability of the samples. Additionally, larger specific surface area can also provide more active reaction sites, so specific surface area is one of the critical factors to the photocatalytic performance enhancement of 60% CBO/BWO nanocomposite [56].

To further understand the specific photo-induced charge separation characteristic of the as-prepared samples, several photo-electrochemical measurements such as PL spectra emission (Fig. 9a), photocurrent response measurement (Fig. 9b) and the electrochemical impedance spectroscopy (EIS) test (Fig. 9c) were also conducted. Generally, PL spectrum is an effective characterization method to investigate the migration, transfer and recombination of the photo-excited electron-hole pairs in semiconductors [57]. It is well recognized that a lower PL intensity implies a lower recombination rate of electron-hole pairs, which leads to higher photocatalytic activity. Fig. 9a presents the PL spectra of pure CBO, BWO and 60% CBO/BWO nanocomposite. Obviously, the main emission peak is centered at about 560 nm for all the samples. The BWO sample possesses the strongest PL emission intensity, indicating the highest recombination rate of electron-hole pairs. Significantly, after the introduction of CBO, the PL emission intensity of 60% CBO/BWO shows a rapid decrease compared to the bare BWO, suggesting that the introduction of CBO can supply more electron-hole capture sites, thus effectively improve the separation efficiency of electron-hole pairs.

The transient photocurrent test of the as-prepared samples was performed in Na_2SO_4 electrolyte under visible-light ($\lambda > 420$ nm) irradiation. Generally, the higher photocurrent response indicates the better separation efficiency of electron-hole pairs [58]. As shown in Fig. 9b, the pure CBO has a very weak light current response of only about 1 $\mu A/cm^2$, and the photocurrent response of pure BWO is slightly higher at about 1.3 $\mu A/cm^2$. The relatively lower photocurrent response represents the higher recombination efficiency of electron-hole pairs in pure CBO and BWO. Compared to the pristine samples, 60% CBO/BWO nanocomposite exhibits the highest photocurrent response reaching at about 8 $\mu A/cm^2$, which further indicates the electron-hole pairs are

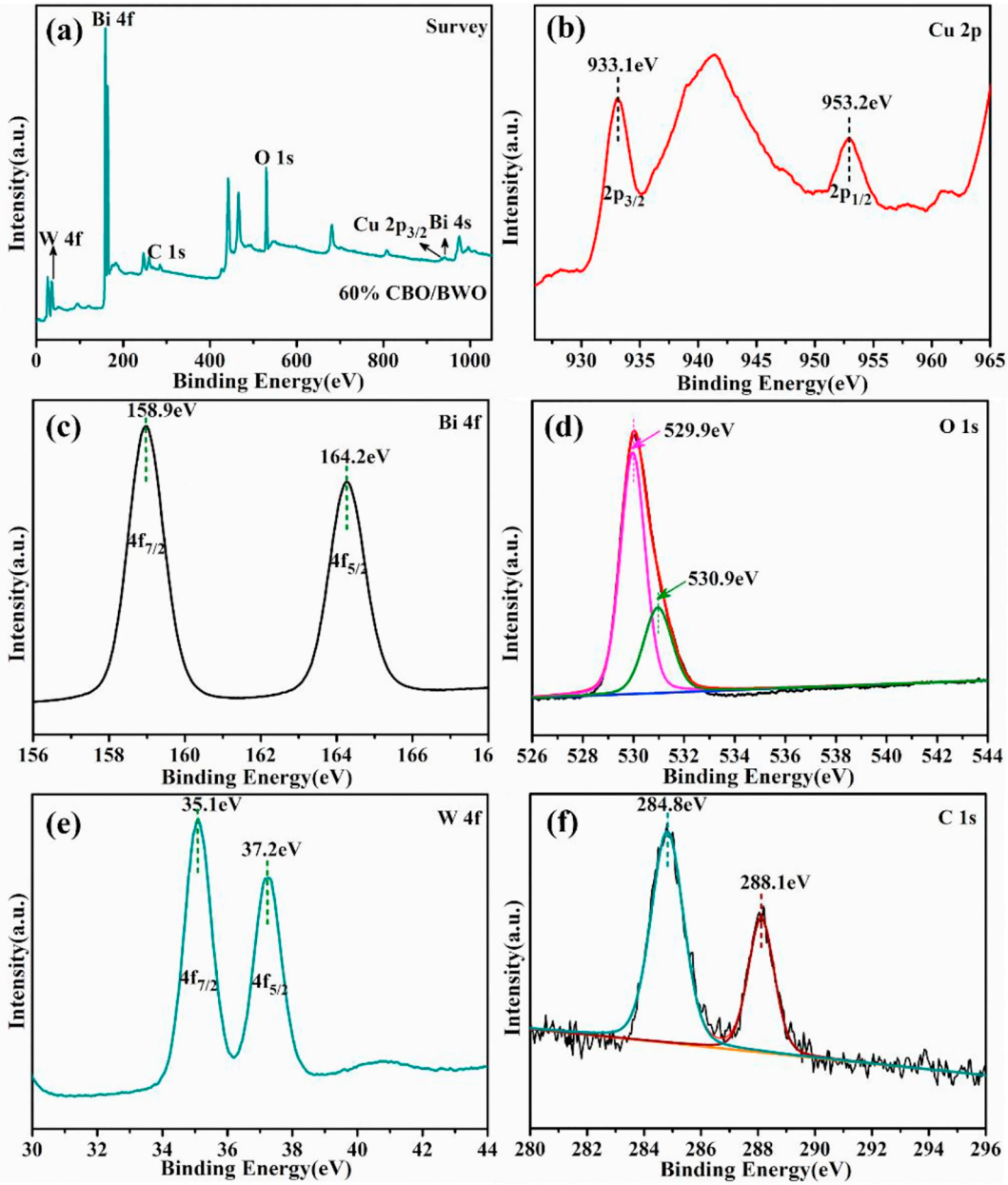

Fig. 5. XPS spectra of 60% CBO/BWO nanocomposite (a) survey spectra of the sample, High resolution XPS spectra of (b) Cu 2p, (c) Bi 4f, (d) O 1s, (e) W4f, (f) C 1s.

effectively separated at the interface between CBO and BWO.

EIS Nyquist plots were also applied to validate the superiority of CBO/BWO nanocomposites over pristine CBO and BWO samples. The arc radius on the EIS spectra reflects the solid state interface layered resistance and the surface charges transfer resistance. Generally, the smaller arc radius represents the smaller impendence, which implies a more efficient separation of the photo-generated electrons and holes [59]. In comparison with the bare BWO and CBO, 60% CBO/BWO nanocomposite displays the smallest arc radius in Fig. 9c, which indicates the resistance on the charge carriers transfer process is significantly reduced. The reduced resistance well-confirms highly effective separation of electron-hole pairs and faster interfacial charge-transfer efficiency in the CBO/BWO nanocomposites [60].

The Bode plot of the phase angle versus frequency for the as-prepared samples was depicted in Fig. 9d. The electron lifetime can be calculated from the following equation [10]:

$$\tau_r = \frac{1}{2\pi f_{peak}} \quad (4)$$

where τ_r is the electron lifetime and f_{peak} is the frequency. In Fig. 9d, the stronger plots of the CBO/BWO nanocomposites mainly located in low-frequency peak area in comparison with the pure CBO and BWO. Therefore, 60% CBO/BWO exhibits the longest electron lifetime. These results further confirm that the combination of CBO and BWO significantly enhances the electron-holes separation [61].

The photocatalytic activity of the as-prepared samples was evaluated by TC photodegradation under visible light illumination. Generally, TC concentration decreased gradually with the increased irradiation time for all samples. As displayed in Fig. 10a, only approximately 6% TC was degraded in the absence of photocatalyst after 60 min visible-light irradiation, indicating that TC was very stable. Both pristine CBO and BWO exhibited poor photocatalytic performance, with the TC degradation efficiency of 36% and 45% after 2-hour reaction. While, after combined these two semiconductors together, all the CBO/BWO nanocomposites displayed much better photocatalytic

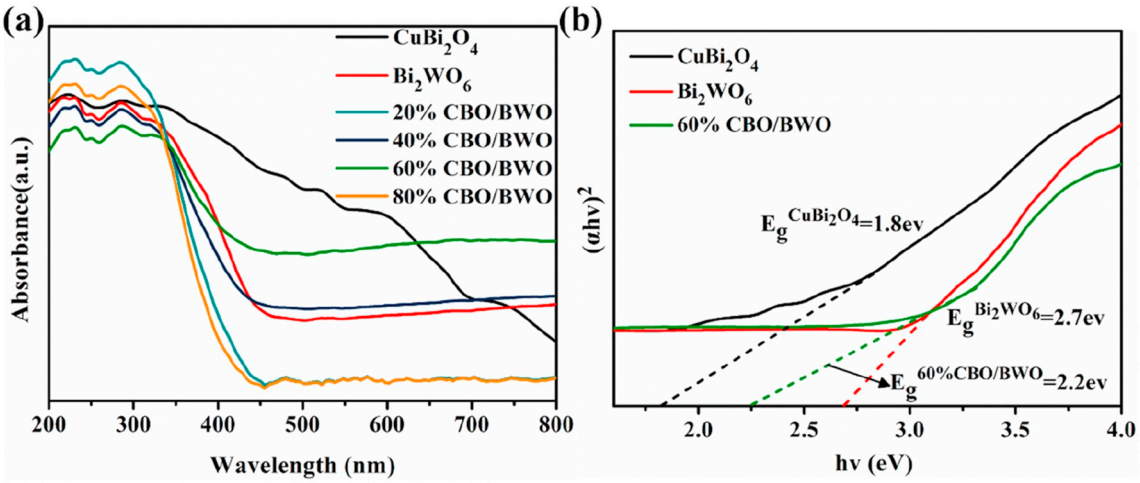

Fig. 6. (a) UV–vis diffuse reflection spectra (DRS) of the as-prepared samples; (b) the plots of $(ah\nu)^{1/2}$ versus photo energy ($h\nu$) of CBO and BWO.

performance than the pristine samples under visible-light irradiation. The photocatalytic performance of the nanocomposites was in the order of 60% CBO/BWO > 80% CBO/BWO > 40% CBO/BWO > 20% CBO/BWO, with the degradation efficiency of 93%, 84%, 83% and 76%, respectively. Apparently, 60% CBO/BWO exhibited the strongest photocatalytic performance over the other ratio nanocomposites, which could degrade 93% TC in 60 min, and almost all the TC was eliminated in 2 h. The first-order kinetics model was used to fit the obtained experimental data in Fig. 10b.

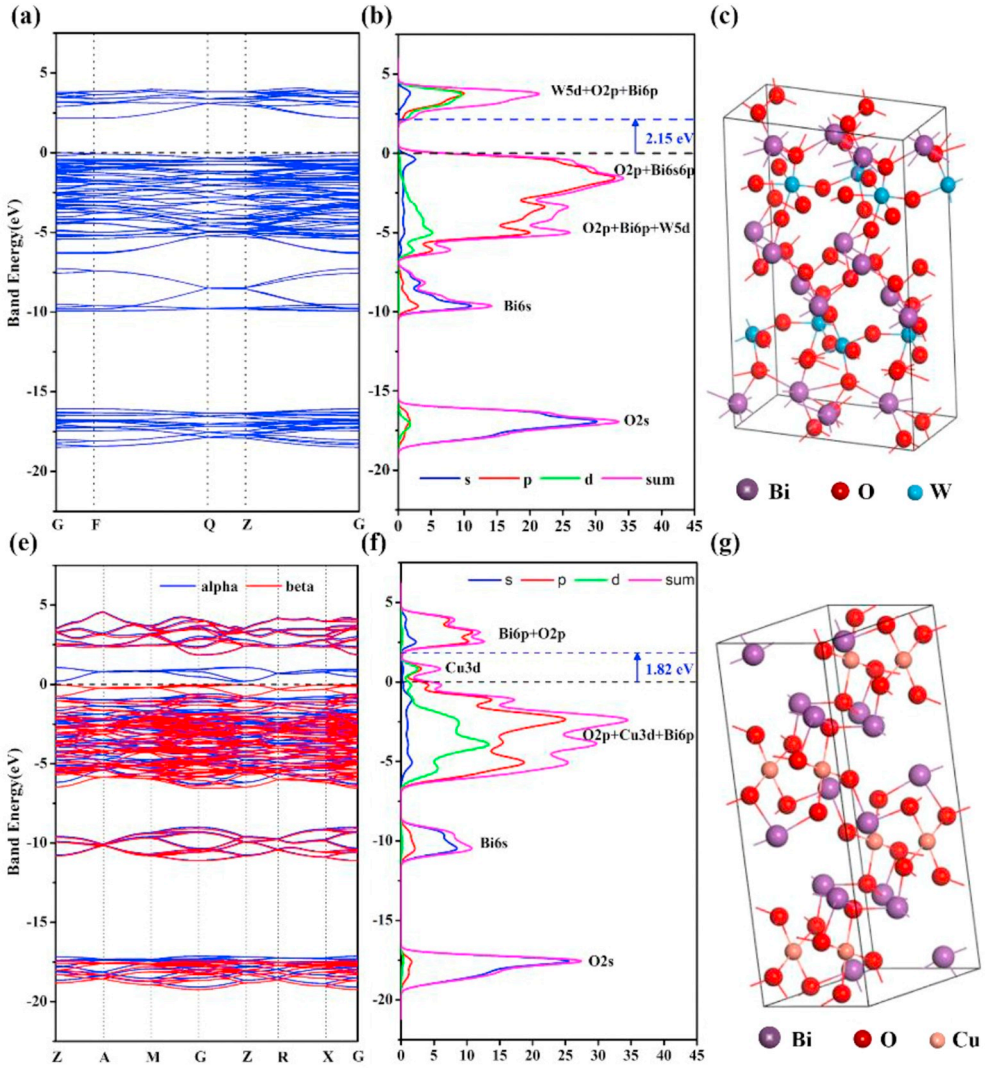

Fig. 7. Energy band diagram of (a) BWO, (e) CBO; Calculated density of states of (b) BWO, (f) CBO; Structure model of (c) BWO, (g) CBO.

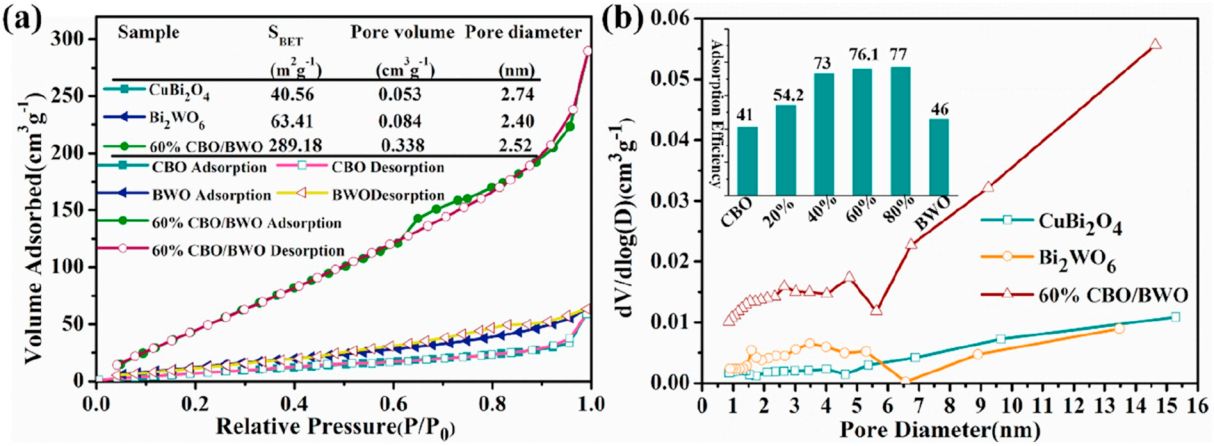

Fig. 8. (a) N_2 adsorption–desorption isotherms of CBO, BWO and 60% CBO/BWO. (b) The corresponding pore size distribution.

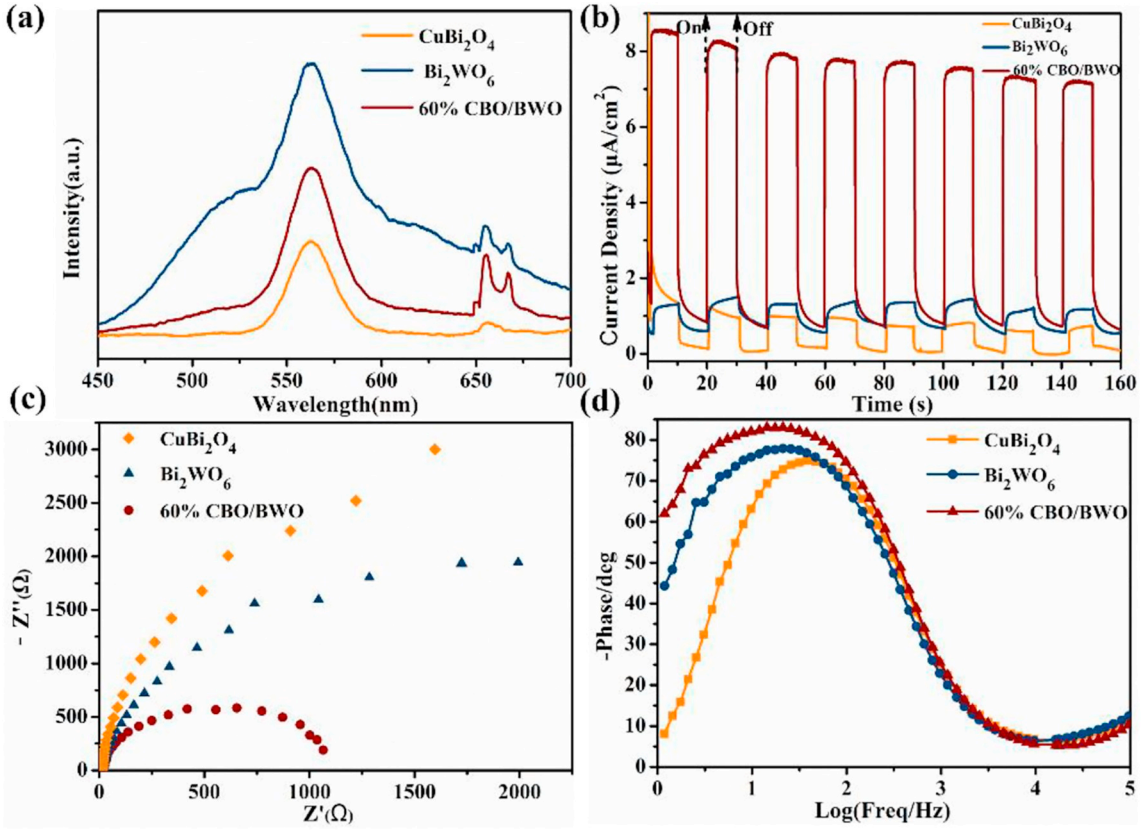

Fig. 9. (a) PL spectra of as-synthesized samples at the excitation wavelength of 325 nm; (b) Plots of photocurrent density vs. irradiation time; (c) EIS Nyquist spectra and (d) Bode EIS plots recorded of pure CBO, BWO and 60% CBO/BWO nanocomposite (at frequency ranging from 1 Hz to 10^5 Hz).

$$\ln \frac{C_0}{C} = kt \tag{5}$$

The corresponding $\ln(C_0/C)$ plots has good linearity property. Fig. 10c demonstrates the corresponding kinetic constants of the as-prepared samples. Apparently, 60% CBO/BWO nanocomposite had the highest k value of 0.0286 min^{-1}, which was almost 7 times higher than that of bare CBO (0.0041 min^{-1}) and BWO (0.0046 min^{-1}). The extraordinary enhanced photocatalytic performance of 60% CBO/BWO nanocomposite can be ascribed to the heterojunction formed on the interface of CBO and BWO. This heterojunction can enhance the visible light response and effectively facilitate the separation of electron-hole pairs. The result has been confirmed by the UV–vis spectra and the PL emission spectra. Additionally, the enlarged specific surface area of the nanocomposites also contributes a lot to the enhanced photocatalytic performance, which is confirmed by the former N_2 adsorption-desorption isotherms.

To ascertain the predominant active species participating in the TC photodegradation reaction, the active species trapping experiments over 60% CBO/BWO nanocomposite were implemented. EDTA-2Na, BQ and IPA were employed as the scavengers of h^+, $\cdot O_2^-$ and $\cdot OH$, respectively [62]. As displayed in Fig. 10d, the degradation efficiency of TC was 92.7% in the absence of scavenger. The addition of 1 mM EDTA slightly inhibited the TC degradation, with degradation efficiency decreased to 71%, indicating h^+ was not the main active specie in the reaction. Whereas, when IPA (1 mM) and BQ (1 mM) were added, the degradation efficiency was dramatically decreased to 24% and 46%,

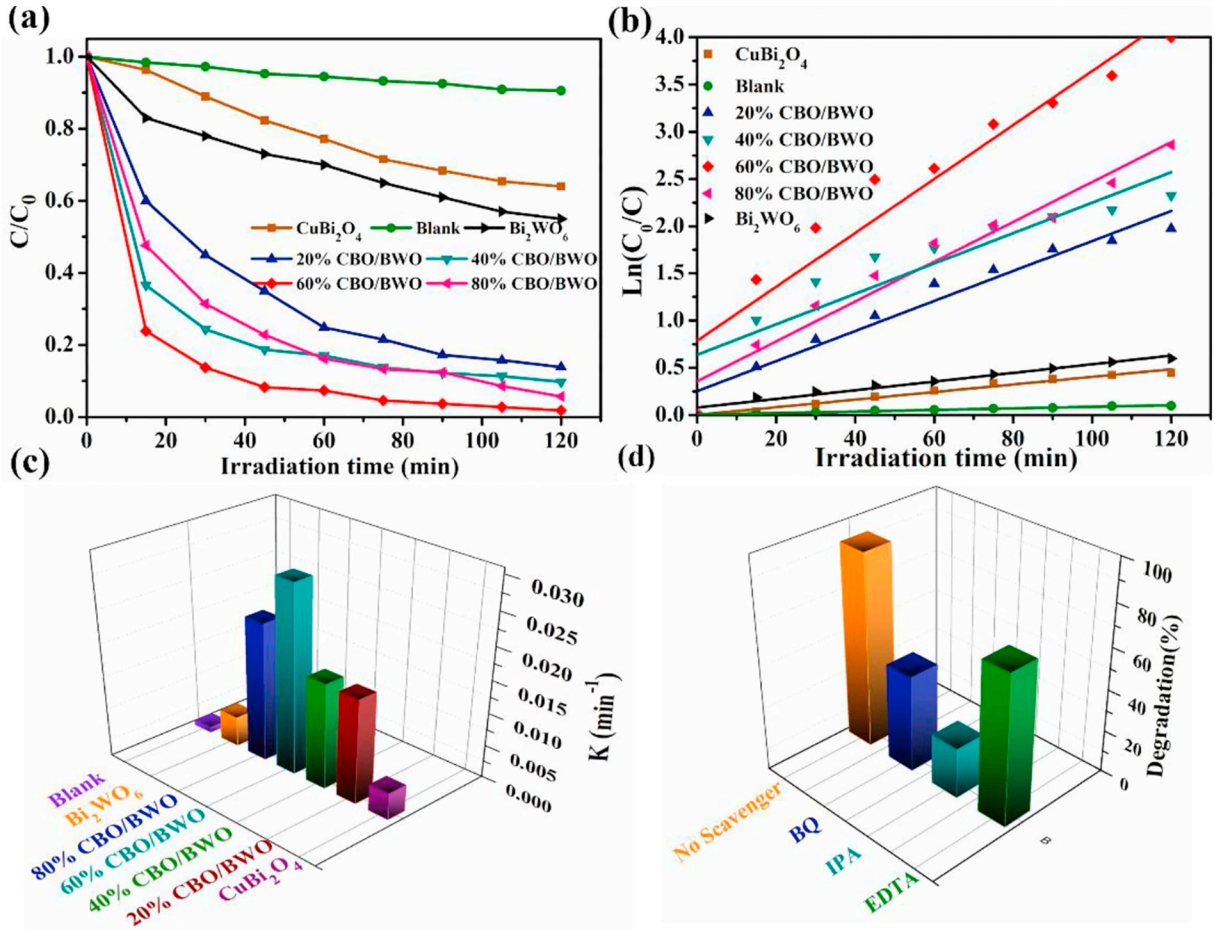

Fig. 10. (a) The photocatalytic activities of the as-prepared samples for TC degradation under visible irradiation (λ > 420 nm). (b) The pseudo-first-order reaction kinetics of the as-prepared samples. (c)The apparent rate constants for TC degradation over the prepared samples. (d) The species trapping experiments for TC degradation over 60% CBO/BWO photocatalyst under visible light irradiation.

respectively, implying the two scavengers greatly inhibited the reaction process. This result suggested that ·OH and ·O2– had a major contribution for the TC degradation over CBO/BWO photocatalyst.

We also measured the chemical oxygen demand (COD) removal in the presence of 60% CBO/BWO nanocomposite in Fig. S1. Based on the COD removal, we calculated the apparent quantum yield (AQY) of the TC photodegradation system in the presence of 60% CBO/BWO photocatalyst, which was 0.32%. The detailed calculation process was in Supplementary Information.

To further confirm the existence of ·OH and $\cdot O_2^-$ and explore the photocatalytic mechanism of the CBO/BWO nanocomposites, the ESR experiment was also conducted [63]. As depicted in Fig. 11a and b, under dark conditions, no obvious peak could be found. However, when CBO/BWO nanocomposite was irradiated with visible light, four characteristic signals of DMPO - ·OH with intensities of 1:2:2:1 appeared in Fig. 11a, and the signals intensities weakened with the increase of irradiation time [64,65]. This result indicated that the ·OH radical was generated in the CBO/BWO system, which can be attributed to the E_{VB} of BWO is positive enough to drive the generation of ·OH. Moreover, six clear signals of $\cdot O_2^-$ were also detected in CBO/BWO nanocomposite under visible light illumination in Fig. 11b, which also proved the presence of $\cdot O_2^-$ in these samples. The ESR results are in great agreement with the results of the trapping experiments, which support that both ·OH and $\cdot O_2^-$ are involved and make great contribution to the enhanced photocatalytic activity of CBO/BWO nanocomposites.

On the basis of these experimental results and the calculated band gap structures, two possible mechanisms of CBO/BWO nanocomposites for the TC degradation were proposed in Fig. 12: (i) traditional heterojunction-type II in Fig. 12a and (ii) Z-scheme type in Fig. 12b. If the charge transfer path follows the traditional type II mechanism (Fig. 12a), the electrons in the CB of CBO will easily transfer to the CB of BWO. Simultaneously, the holes will migrate from the VB of BWO to that of CBO. The motivation of the transportation is the potential difference between them. Consequently, the electrons will accumulate in the CB of BWO, and the holes will accumulate in the VB of CBO. However, the accumulated electrons in the CB of BWO cannot react with the adsorbed O_2 to produce $\cdot O_2^-$, because the CB level (0.54 eV vs. NHE) of BWO is more positive than the $O_2/\cdot O_2^-$ potential (–0.33 eV vs. NHE). Moreover, the accumulated holes in the VB of CBO cannot oxidize OH^- or H_2O into ·OH, because the VB potential (1.15 eV vs. NHE) of CBO is more negative than the standard $OH^-/\cdot OH$ (1.99 eV vs. NHE) and $H_2O/\cdot OH$ (2.74 eV vs. NHE) potential [66]. However, this presumption is contradictory to the reactive species trapping and ESR results, in which ·OH and $\cdot O_2^-$ radicals are testified to be the predominant species in the photocatalytic reaction. Therefore, a more reasonable Z-scheme mechanism is proposed in Fig. 12b. In the Z-scheme mechanism, the photo-generated electrons in the CB of BWO will trendily migrate to the VB of CBO, and then it will recombine with the holes in VB of CBO. The photo-induced electrons left at the CB of CBO possess strong reduction potential (–0.65 eV vs. NHE) to capture and reduce the dissolved O_2 into $\cdot O_2^-$. Additionally, the holes left at the CB of BWO have strong oxidation ability which can directly oxidize TC into harmless products. Furthermore, the holes potential level (3.24 eV vs. NHE) at the CB of BWO is positive enough to oxidize H_2O

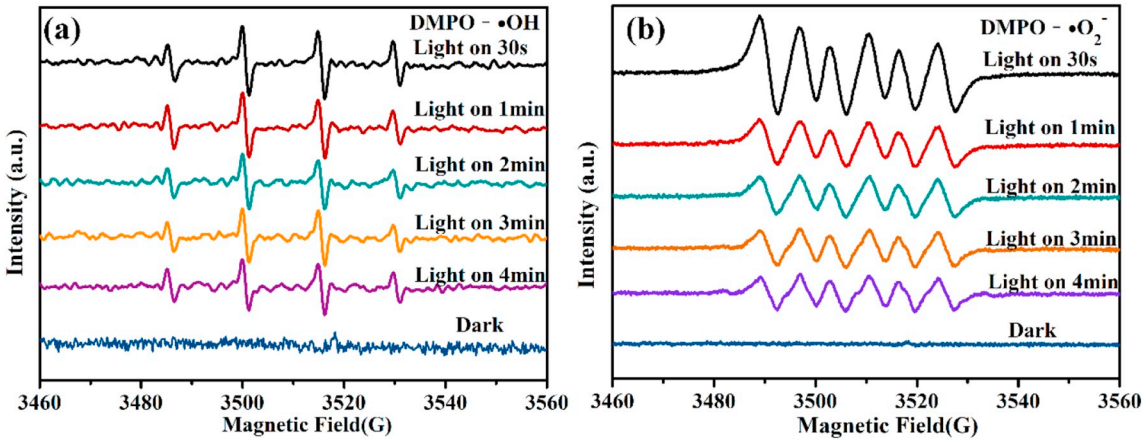

Fig. 11. DMPO spin-trapping ESR spectra of 60% CBO/BWO nanocomposite (a)in aqueous dispersion (for DMPO-·OH) methanol dispersion and (b) in methanol dispersion (for DMPO - $\cdot O_2^-$) under visible light irradiation ($\lambda > 420$ nm).

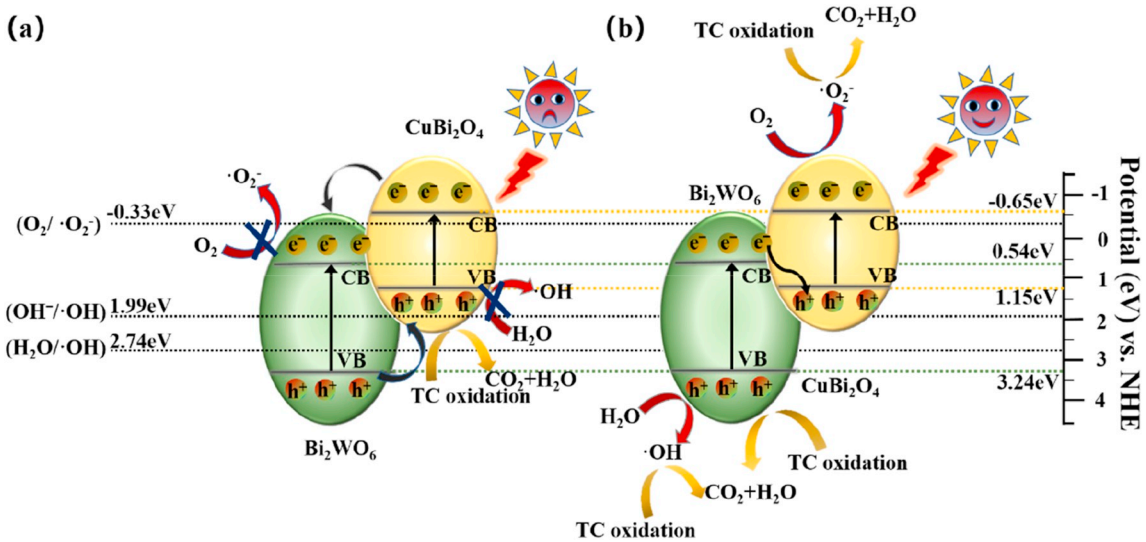

Fig. 12. Two models of charge separation proposed for CBO/BWO nanocomposites under visible irradiation: traditional heterojunction-type II (a) and Z-scheme type (b).

into ·OH [67]. The Z-scheme mechanism is in well agreement with the trapping and ESR experiments results, in which ·OH and $\cdot O_2^-$ are existed in the CBO/BWO system and play an important role in the photocatalytic reaction. Therefore, the Z-scheme mechanism effectively facilitates the separation of electron-hole pairs, and retains the electrons' strong redox power in the more negative CB of CBO and the holes' strong oxidation power in the more positive VB of BWO. These advantages make CBO/BWO nanocomposites exhibiting extraordinary photocatalytic performance for TC photodegradation. The mechanism for the TC photo-degradation can be explained as follows [68]:

$$CBO + h\nu \rightarrow e_{CB}^- + h_{VB}^+ \quad (6)$$

$$BWO + h\nu \rightarrow e_{CB}^- + h_{VB}^+ \quad (7)$$

$$O_2 + e_{CB}^- \rightarrow \cdot O_2^- \quad (8)$$

$$\cdot O_2^- + 2H^+ \rightarrow H_2O_2 \quad (9)$$

$$OH^- + h_{VB}^+ \rightarrow \cdot OH \quad (10)$$

$$H_2O + h_{VB}^+ \rightarrow \cdot OH + H^+ \quad (11)$$

$$TC + \cdot OH/\cdot O_2^-/H_2O_2 \rightarrow H_2O + CO_2 + \text{products} \quad (12)$$

4. Conclusion

In summary, we constructed the Z-scheme $CuBi_2O_4/Bi_2WO_6$ hierarchical nanocomposites via a facile hydrothermal method. Compared to the bare CBO and BWO, the as-synthesized CBO/BWO nanocomposites exhibited enhanced photocatalytic activities toward TC degradation under visible light irradiation. The apparent rate constant for 60% CBO/BWO sample ($0.0286\ min^{-1}$) was approximately 7 times higher than that of the pristine sample. The enhanced photocatalytic performance was mainly attributed to the unique Z-scheme heterojunction, which consequently leaded to the suppressed charge recombination and efficient charge transfer in the interface. The higher electrons' reduction potential in CBOs' CB and the stronger holes' oxidation potential in BWOs' VB were also retained. The enlarged specific surface area and the increased visible light adsorption also benefited the improved photocatalytic performance. Moreover, the radical trapping and ESR experiments results indicated that ·OH and $\cdot O_2^-$ were the predominant species. Specifically, the charge transfer route was discussed in detail, and the heterojunction in CBO/BWO nanocomposites following Z-scheme type was convinced. The DFT calculations suggested that for CBO, the p-d transition occurred from the valence band formed by the O2p orbital to the conduction band formed by the Cu3d orbital. For BWO, photoexcitation electrons transferred from the valence band of

O2p + Bi6s hybrid orbitals to the conduction band of W5d orbital. Based on the DFT calculations, we reasonably convince that the photoexcitation electrons transferred from the W5d orbital of BWO's CB to the O2p orbital of CBO's VB in the Z-scheme CBO/BWO nanocomposite system.

Acknowledgements

The authors gratefully acknowledge the financial support provided by the China Scholarship Council (No. 201806560036, No. 201806050172), Shaanxi Provincial Natural Science Foundation of China (No. 2018JM2030, No. 2017JM2014), the National Natural Science Foundation of China (No. 21806128), and National College Students Innovation and Entrepreneurship Training Program (No. 201810710102, No. 201810710269). This work was also supported by the Brook Byers Institute for Sustainable Systems in Georgia Institute of Technology.

Appendix A. Supplementary data

Supplementary data to this article can be found online at https://doi.org/10.1016/j.apsusc.2019.07.263.

References

[1] S. Adhikari, S. Selvaraj, D.-H. Kim, Construction of heterojunction photoelectrode via atomic layer deposition of Fe_2O_3 on Bi_2WO_6 for highly efficient photoelectrochemical sensing and degradation of tetracycline, Appl. Catal. B Environ. 244 (2019) 11–24.
[2] M. Thaker, P. Spanogiannopoulos, G.D. Wright, The tetracycline resistome, Cell. Mol. Life Sci. 67 (2010) 419–431.
[3] R. Daghrir, P. Drogui, Tetracycline antibiotics in the environment: a review, Environ. Chem. Lett. 11 (2013) 209–227.
[4] I. Chopra, M. Roberts, Tetracycline antibiotics: mode of action, applications, molecular biology, and epidemiology of bacterial resistance, Microbiol. Mol. Biol. Rev. 65 (2001) 232.
[5] M.E. Parolo, M.C. Savini, J.M. Vallés, M.T. Baschini, M.J. Avena, Tetracycline adsorption on montmorillonite: pH and ionic strength effects, Appl. Clay Sci. 40 (2008) 179–186.
[6] F. Ferrag-Siagh, F. Fourcade, I. Soutrel, H. Aït-Amar, H. Djelal, A. Amrane, Tetracycline degradation and mineralization by the coupling of an electro-Fenton pretreatment and a biological process, J. Chem. Technol. Biotechnol. 88 (2013) 1380–1386.
[7] I. Koyuncu, O.A. Arikan, M.R. Wiesner, C. Rice, Removal of hormones and antibiotics by nanofiltration membranes, J. Membr. Sci. 309 (2008) 94–101.
[8] W. Shi, F. Guo, M. Li, Y. Shi, M. Shi, C. Yan, Constructing 3D sub-micrometer CoO octahedrons packed with layered MoS_2 shell for boosting photocatalytic overall water splitting activity, Appl. Surf. Sci. 473 (2019) 928–933.
[9] Y. Zeng, H. Li, J. Luo, J. Yuan, L. Wang, C. Liu, Y. Xia, M. Liu, S. Luo, T. Cai, S. Liu, J.C. Crittenden, Sea-urchin-structure g-C_3N_4 with narrow bandgap (2.0 eV) for efficient overall water splitting under visible light irradiation, Appl. Catal. B Environ. 249 (2019) 275–281.
[10] M. Guo, K. Xie, J. Lin, Z. Yong, C.T. Yip, L. Zhou, Y. Wang, H. Huang, Design and coupling of multifunctional TiO_2 nanotube photonic crystal to nanocrystalline titania layer as semi-transparent photoanode for dye-sensitized solar cell, Energy Environ. Sci. 5 (2012) 9881.
[11] M. Baek, E.J. Kim, S.W. Hong, W. Kim, K. Yong, Environmentally benign synthesis of CuInS$_2$/ZnO heteronanorods: visible light activated photocatalysis of organic pollutant/bacteria and study of its mechanism, Photochem Photobiol Sci 16 (2017) 1792–1800.
[12] W. Lian-Jun, L.U.O. Wei, J. Wan, L.I.U. Jia-Le, C. Dong, Z. Bei-Ying, Preparation and property of CuInS$_2$/ZnS core-shell quantum dots in aqueous phase, J. Inorg. Mater. 33 (2018) 279.
[13] L. Jiang, X. Yuan, G. Zeng, J. Liang, X. Chen, H. Yu, H. Wang, Z. Wu, J. Zhang, T. Xiong, In-situ synthesis of direct solid-state dual Z-scheme WO_3/g-C_3N_4/Bi_2O_3 photocatalyst for the degradation of refractory pollutant, Appl. Catal. B Environ. 227 (2018) 376–385.
[14] J. Xu, W. Wang, S. Sun, L. Wang, Enhancing visible-light-induced photocatalytic activity by coupling with wide-band-gap semiconductor: a case study on Bi_2WO_6/TiO_2, Appl. Catal. B Environ. 111-112 (2012) 126–132.
[15] L. Ge, C. Han, J. Liu, Novel visible light-induced g-C_3N_4/Bi_2WO_6 composite photocatalysts for efficient degradation of methyl orange, Appl. Catal. B Environ. 108-109 (2011) 100–107.
[16] K. Lai, Y. Zhu, J. Lu, Y. Dai, B. Huang, N- and Mo-doping Bi_2WO_6 in photocatalytic water splitting, Comput. Mater. Sci. 67 (2013) 88–92.
[17] W. Dai, H. Xu, J. Yu, X. Hu, X. Luo, X. Tu, L. Yang, Photocatalytic reduction of CO_2 into methanol and ethanol over conducting polymers modified Bi_2WO_6 microspheres under visible light, Appl. Surf. Sci. 356 (2015) 173–180.
[18] Y. Zhu, Y. Wang, Q. Ling, Y. Zhu, Enhancement of full-spectrum photocatalytic activity over $BiPO_4$/Bi_2WO_6 composites, Appl. Catal. B Environ. 200 (2017) 222–229.
[19] W. Guo, K. Fan, J. Zhang, C. Xu, 2D/2D Z-scheme Bi_2WO_6/porous-g-C_3N_4 with synergy of adsorption and visible-light-driven photodegradation, Appl. Surf. Sci. 447 (2018) 125–134.
[20] J. Wang, L. Tang, G. Zeng, Y. Deng, H. Dong, Y. Liu, L. Wang, B. Peng, C. Zhang, F. Chen, 0D/2D interface engineering of carbon quantum dots modified Bi_2WO_6 ultrathin nanosheets with enhanced photoactivity for full spectrum light utilization and mechanism insight, Appl. Catal. B Environ. 222 (2018) 115–123.
[21] W. Shi, F. Guo, M. Li, Y. Shi, M. Wu, Y. Tang, Enhanced visible-light-driven photocatalytic H_2 evolution on the novel nitrogen-doped carbon dots/$CuBi_2O_4$ microrods composite, J. Alloys Compd. 775 (2019) 511–517.
[22] M. Liu, M.B. Johnston, H.J. Snaith, Efficient planar heterojunction perovskite solar cells by vapour deposition, Nature 501 (2013) 395–398.
[23] Q. Xu, L. Zhang, J. Yu, S. Wageh, A. Al-Ghamdi, M. Jaroniec, Direct Z-scheme photocatalysts: principles, synthesis, and applications, Mater. Today 21 (2018) 1042–1063.
[24] J. Low, B. Dai, T. Tong, C. Jiang, J. Yu, In situ irradiated X-ray photoelectron spectroscopy investigation on a direct Z-scheme TiO_2/CdS composite film Photocatalyst, Adv. Mater. 31 (2019) 1802981.
[25] Z. Chen, W. Wang, Z. Zhang, X. Fang, High-efficiency visible-light-driven Ag_3PO_4/AgI photocatalysts: Z-scheme photocatalytic mechanism for their enhanced photocatalytic activity, J. Phys. Chem. C 117 (2013) 19346–19352.
[26] R. He, J. Zhou, H. Fua, S. Zhang, C. Jiang, Room-temperature in situ fabrication of Bi_2O_3/g-C_3N_4 direct Z-scheme photocatalyst with enhanced photocatalytic activity, Appl. Surf. Sci. 430 (2018) 273–282.
[27] Y. Gong, X. Quan, H. Yu, S. Chen, H. Zhao, Enhanced photocatalytic performance of a two-dimensional $BiOIO_3$/g-C_3N_4 heterostructured composite with a Z-scheme configuration, Appl. Catal. B Environ. 237 (2018) 947–956.
[28] Z. Wei, F. Yue, H. Haibao, Z. Pengcheng, L. Jing, Z. Lili, D. Benlin, X. Jiming, Z. Fengxia, S. Ni, D.Y.C. Leung, A novel Z-scheme Ag_3VO_4/$BiVO_4$ heterojunction photocatalyst: study on the excellent photocatalytic performance and photocatalytic mechanism, Appl. Catal. B Environ. 245 (2019) 448–458.
[29] Y. Sua, G. Tan, T. Liu, L. Lv, Y. Wang, Photocatalytic properties of Bi_2WO_6/$BiPO_4$ Z-scheme photocatalysts induced by double internal electric fields, Appl. Surf. Sci. 457 (2018) 104–114.
[30] Y. Wang, S. Jiang, F. Liu, C. Zhao, D. Zhao, X. Li, Study on preparation and toluene removal of BiOI/Bi_2WO_6/ACF photocatalyst, Appl. Surf. Sci. 488 (2019) 161–169.
[31] F. Wang, W. Septina, A. Chemseddine, F.F. Abdi, D. Friedrich, P. Bogdanoff, R. van de Krol, S.D. Tilley, S.P. Berglund, Gradient self-doped $CuBi_2O_4$ with highly improved charge separation efficiency, J. Am. Chem. Soc. 139 (2017) 15094–15103.
[32] Y. Wang, H. Wang, A.R. Woldu, X. Zhang, T. He, Optimization of charge behavior in nanoporous $CuBi_2O_4$ photocathode for photoelectrochemical reduction of CO_2, Catal. Today 335 (2018) 388–394.
[33] J. Deng, Y.-q. Cheng, Y.-a. Lu, J.C. Crittenden, S.-q. Zhou, N.-y. Gao, J. Li, Mesoporous manganese cobaltite nanocages as effective and reusable heterogeneous peroxymonosulfate activators for carbamazepine degradation, Chem. Eng. J. 330 (2017) 505–517.
[34] J. Deng, S. Feng, K. Zhang, J. Li, H. Wang, T. Zhang, X. Ma, Heterogeneous activation of peroxymonosulfate using ordered mesoporous Co_3O_4 for the degradation of chloramphenicol at neutral pH, Chem. Eng. J. 308 (2017) 505–515.
[35] F. Dong, C. Li, J. Crittenden, T. Zhang, Q. Lin, G. He, W. Zhang, J. Luo, Sulfadiazine destruction by chlorination in a pilot-scale water distribution system: kinetics, pathway, and bacterial community structure, J. Hazard. Mater. 366 (2019) 88–97.
[36] W. Yu, J. Chen, T. Shang, L. Chen, L. Gu, T. Peng, Direct Z-scheme g-C_3N_4/WO_3 photocatalyst with atomically defined junction for H_2 production, Appl. Catal. B Environ. 219 (2017) 693–704.
[37] W. Shi, F. Guo, S. Yuan, In situ synthesis of Z-scheme Ag_3PO_4/$CuBi_2O_4$ photocatalysts and enhanced photocatalytic performance for the degradation of tetracycline under visible light irradiation, Appl. Catal. B Environ. 209 (2017) 720–728.
[38] Y. Li, L. Chen, Y. Wang, L. Zhu, Advanced nanostructured photocatalysts based on reduced graphene oxide-flower-like Bi_2WO_6 composites for an augmented simulated solar photoactivity activity, Mater. Sci. Eng. B 210 (2016) 29–36.
[39] J. Tian, Y. Sang, G. Yu, H. Jiang, X. Mu, H. Liu, A Bi_2WO_6-based hybrid photocatalyst with broad spectrum photocatalytic properties under UV, visible, and near-infrared irradiation, Adv. Mater. 25 (2013) 5075–5080.
[40] H. Khan, M.G. Rigamonti, G.S. Patience, D.C. Boffito, Spray dried TiO_2/WO_3 heterostructure for photocatalytic applications with residual activity in the dark, Appl. Catal. B Environ. 226 (2018) 311–323.
[41] J. Zhu, J.-G. Wang, Z.-F. Bian, F.-G. Cao, H.-X. Li, Solvothermal synthesis of highly active Bi_2WO_6 visible photocatalyst, Res. Chem. Intermed. 35 (2009) 799–806.
[42] F. He, Z. He, J. Xie, Y. Li, IR and Raman spectra properties of Bi_2O_3-ZnO-B_2O_3-BaO quaternary glass system, Am. J. Anal. Chem. 05 (2014) 1142–1150.
[43] A. Radhakrishnan, B. Beena Structural, Optical absorption analysis of CuO nanoparticles, Indian Journal of Advances in Chemical Science 2 (2) (2014) 158–161.
[44] F. Wang, H. Yang, Y. Zhang, Enhanced photocatalytic performance of $CuBi_2O_4$ particles decorated with Ag nanowires, Mater. Sci. Semicond. Process. 73 (2018) 58–66.
[45] Z. Zhu, Y. Ren, Q. Li, H. Liu, H. Weng, One-pot electrodeposition synthesis of Bi_2WO_6/graphene composites for photocatalytic applications under visible light irradiation, Ceram. Int. 44 (2018) 3511–3516.
[46] L. Zhang, H. Wang, Z. Chen, P.K. Wong, J. Liu, Bi_2WO_6 micro/nano-structures: synthesis, modifications and visible-light-driven photocatalytic applications, Appl. Catal. B Environ. 106 (2011) 1–13.
[47] T. Xie, Y. Liu, H. Wang, Z. Wu, Layered $MoSe_2$/Bi_2WO_6 composite with P-N

heterojunctions as a promising visible-light induced photocatalyst, Appl. Surf. Sci. 444 (2018) 320–329.
[48] E. Abdelkader, L. Nadjia, B. Ahmed, Synthesis, characterization and UV-A light photocatalytic activity of 20wt%SrO–CuBi2O4 composite, Appl. Surf. Sci. 258 (2012) 5010–5024.
[49] M. Chen, Q. Yang, L. Li, M. Liu, P. Xiao, M. Zhang, Solid-state synthesis of $CuBi_2O_4$/MWCNT composites with enhanced photocatalytic activity under visible light irradiation, Mater. Lett. 171 (2016) 255–258.
[50] Y. Deng, Y. Chen, B. Chen, J. Ma, Preparation, characterization and photocatalytic activity of $CuBi_2O_4$/$NaTaO_3$ coupled photocatalysts, J. Alloys Compd. 559 (2013) 116–122.
[51] F. Guo, W. Shi, H. Wang, M. Han, W. Guan, H. Huang, Y. Liu, Z. Kang, Study on highly enhanced photocatalytic tetracycline degradation of type AgI/$CuBi_2O_4$ and Z-scheme AgBr/$CuBi_2O_4$ heterojunction photocatalysts, J. Hazard. Mater. 349 (2018) 111–118.
[52] H. Fu, C. Pan, W. Yao, Y. Zhu, Visible-light-induced degradation of rhodamine B by nanosized Bi_2WO_6, J. Phys. Chem. B 109 (2005) 22432–22439.
[53] K. Lai, W. Wei, Y. Dai, R. Zhang, B. Huang, DFT calculations on structural and electronic properties of Bi_2MO_6 (M = Cr, Mo, W), Rare Metals 30 (2011) 166–172.
[54] D. Lu, M. Yang, K.K. Kumar, H. Wang, X. Zhao, P. Wu, P. Fang, Grape-like Bi_2WO_6/CeO_2 hierarchical microspheres: a superior visible-light-driven photoelectric efficiency with magnetic recycled characteristic, Sep. Purif. Technol. 194 (2018) 130–134.
[55] L. Deng, H. Zeng, Z. Shi, W. Zhang, J. Luo, Sodium dodecyl sulfate intercalated and acrylamide anchored layered double hydroxides: a multifunctional adsorbent for highly efficient removal of Congo red, J. Colloid Interface Sci. 521 (2018) 172–182.
[56] L. Jiang, X. Yuan, G. Zeng, X. Chen, Z. Wu, J. Liang, J. Zhang, H. Wang, H. Wang, Phosphorus- and sulfur-codoped g-C_3N_4: facile preparation, mechanism insight, and application as efficient photocatalyst for tetracycline and methyl orange degradation under visible light irradiation, ACS Sustain. Chem. Eng. 5 (2017) 5831–5841.
[57] Y. Bao, K. Chen, Novel Z-scheme BiOBr/reduced graphene oxide/protonated g-C_3N_4 photocatalyst: synthesis, characterization, visible light photocatalytic activity and mechanism, Appl. Surf. Sci. 437 (2018) 51–61.
[58] Y. Hong, Y. Jiang, C. Li, W. Fan, X. Yan, M. Yan, W. Shi, In-situ synthesis of direct solid-state Z-scheme V_2O_5/g-C_3N_4 heterojunctions with enhanced visible light efficiency in photocatalytic degradation of pollutants, Appl. Catal. B Environ. 180 (2016) 663–673.
[59] J. Safaei, H. Ullah, N.A. Mohamed, M.F. Mohamad Noh, M.F. Soh, A.A. Tahir, N. Ahmad Ludin, M.A. Ibrahim, W.N.R. Wan Isahak, M.A. Mat Teridi, Enhanced photoelectrochemical performance of Z-scheme g-C_3N_4/$BiVO_4$ photocatalyst, Appl. Catal. B Environ. 234 (2018) 296–310.
[60] H. Lahmar, F. Setifi, A. Azizi, G. Schmerber, A. Dinia, On the electrochemical synthesis and characterization of p-Cu_2O/n-ZnO heterojunction, J. Alloys Compd. 718 (2017) 36–45.
[61] N. Xu, F. Li, L. Gao, H. Hu, Y. Hu, X. Long, J. Ma, J. Jin, N,Cu-codoped carbon nanosheet/Au/$CuBi_2O_4$ photocathodes for efficient photoelectrochemical water splitting, ACS Sustain. Chem. Eng. 6 (2018) 7257–7264.
[62] Z. Wu, X. Yuan, H. Wang, Z. Wu, L. Jiang, H. Wang, L. Zhang, Z. Xiao, X. Chen, G. Zeng, Facile synthesis of a novel full-spectrum-responsive $Co_{2.67}S_4$ nanoparticles for UV-, vis- and NIR-driven photocatalysis, Appl. Catal. B Environ. 202 (2017) 104–111.
[63] F. Chen, Q. Yang, J. Sun, F. Yao, S. Wang, Y. Wang, X. Wang, X. Li, C. Niu, D. Wang, G. Zeng, Enhanced photocatalytic degradation of tetracycline by AgI/$BiVO_4$ heterojunction under visible-light irradiation: mineralization efficiency and mechanism, ACS Appl. Mater. Interfaces 8 (2016) 32887–32900.
[64] H. Yu, B. Huang, H. Wang, X. Yuan, L. Jiang, Z. Wu, J. Zhang, G. Zeng, Facile construction of novel direct solid-state Z-scheme AgI/BiOBr photocatalysts for highly effective removal of ciprofloxacin under visible light exposure: mineralization efficiency and mechanisms, J. Colloid Interface Sci. 522 (2018) 82–94.
[65] H. Huang, X. Li, J. Wang, F. Dong, P.K. Chu, T. Zhang, Y. Zhang, Anionic group self-doping as a promising strategy: band-gap engineering and multi-functional applications of high-performance CO_{32}–doped $Bi_2O_2CO_3$, ACS Catal. 5 (2015) 4094–4103.
[66] D. Xu, B. Cheng, S. Cao, J. Yu, Enhanced photocatalytic activity and stability of Z-scheme Ag_2CrO_4-GO composite photocatalysts for organic pollutant degradation, Appl. Catal. B Environ. 164 (2015) 380–388.
[67] X. Liu, L. Cai, Novel indirect Z-scheme photocatalyst of Ag nanoparticles and polymer polypyrrole co-modified BiOBr for photocatalytic decomposition of organic pollutants, Appl. Surf. Sci. 445 (2018) 242–254.
[68] Z. Duan, L. Deng, Z. Shi, H. Zhang, H. Zeng, J. Crittenden, In situ growth of Ag-SnO_2 quantum dots on silver phosphate for photocatalytic degradation of carbamazepine: performance, mechanism and intermediates toxicity assessment, J. Colloid Interface Sci. 534 (2019) 270–278.